Dimensioning of a traction motor for the FST using a Vanadium-Cobalt-Iron alloy

António C. Cardoso
Técnico Lisboa
University of Lisbon,
1049-001 Lisbon, Portugal
antonio.c.cardoso@tecnico.ulisboa.pt

October 2020

***Abstract*—Hybrid and fully electric vehicles have pursued a recent growth and, along with this, new electric machines technologies are being developed focusing on increasing efficiency and specific power through the application of optimisation techniques and new materials. In this work, a high specific-power spoke-type Interior Permanent Magnet Synchronous Machine (IPMSM) for the competition's Formula Student Técnico (FST) electric car has been optimised, demanding high-performance requirements with a large ratio of power/volume. Two different magnetic materials were tested for the motor's magnetic core: the typical Silicon-Iron alloy (FeSi) and a Vanadium-Cobalt-Iron alloy (VCoFe) alloy. This project attempts to define in which conditions the VCoFe alloy, holding a remarkable high saturation point of 2.2-2.4 T, provides advantages in this application, over the FeSi. Multi-objective optimisation was developed to identify the best parameters and machine designs, using VCoFe and FeSi, regarding specific power and efficiency, while fulfilling the relevant applicable constraints. The optimisation was done using the Non-dominated Sorting Genetic Algorithm II (NSGA-II) algorithm coupled with a hybrid analytical/finite element method to provide sufficiently accurate electromagnetic and thermal results within a feasible time. Results demonstrate VCoFe as a beneficial core material, providing higher specific power than FeSi. Outperforming FeSi in an estimated increase of up to 3% in efficiency for the same torque, or up to 70% torque increase for the same efficiency level. For the FST competition car, with a required 20 Nm of nominal torque, there is an efficiency increase of 1.7% and a reduction of 11% in core volume for the motor.**

***Index Terms*—Electric vehicle, Electromagnetic modelling, Finite element method, Multi-objective optimisation, Permanent magnet synchronous machine, Silicon-Iron, Vanadium-Cobalt-Iron.**

I Introduction

Electric Vehicle (EV) is today present in the motor-sport environment, with the adoption of hybrid systems in Formula 1 and the development of Formula E exclusively for electric race cars. These competitions provide an opportunity to test and validate state-of-the-art technologies and to analyse the possibility of integrating them into passenger's road cars. Within this context, this project aims to design and optimise a spoke-type Interior Permanent Magnet Synchronous Machine (IPMSM) for a vehicle of Formula Student Técnico (FST) competitions with a non-conventional material as magnetic core material to contribute to the research and development of high-performance Electrical Machine (EM) and Electric Vehicles (EV).

The focus on increasing efficiency and specific power in new EM's technologies is a continuous quest within the research and industrial communities. With the development of new approaches to the EM's design and manufacturing, higher efficiency and lighter EMs are now reachable. This led to great advantages in applications where weight, volume and efficiency are key aspects, as in traction applications of electric mobility and transportation. With this purpose, an approach to produce optimised EMs was done, applying new soft-magnetic materials to the EM's magnetic core to spread current electromagnetic limits and optimising existent topologies.

Vanadium-Cobalt-Alloy (VCoFe) is the soft-magnetic material tested in this project to be compared against the typical Silicon-Iron (FeSi) alloy. VCoFe is defined by a high saturation point of 2.2-2.4 T [1] and, bearing this, it has been emerging as one potential candidate to expand current electromagnetic limits of EMs, regarding its power density and efficiency [2]. Although, its higher magnetic densities may lead to a higher contribution of losses and consequently, the pursuit whereas the achievable reduced core volume is enough to, for the same power, maintain higher efficiency values than the typical FeSi magnetic cores is essential. The thermal behaviour has also high influence in the motor design, not only it may determine if a design is viable or not, due to each material's withstanding temperature, but it also becomes significant as higher magnetic core losses may prevent the full use of VCoFe's high magnetic flux density.

Several studies have established benefits on using VCoFe as the magnetic core material of EMs for high-speed traction applications and aerospace applications to increase the specific-power of Synchronous Reluctance Machine (SRM) [3–5] and Permanent Magnet Synchronous Machine (PMSM) [6, 7]. Concerning EV traction applications, the use of VCoFe has been a minor success compared with FeSi, although [2, 8] account with an increase of at least 20% in torque/specific-power.

A previous FST competition car powertrain has been designed with a high-performance spoke-type IPMSM using

FeSi as magnetic core material [9]. This project accomplished the manufacturing and validation of the motor through experimental testing where VCoFe is considered as a promising material to improve the performance of the FST car. The spoke-type IPMSM topology was opted for the powertrain of the FST's car since it is an advantage due to the higher concentration of magnetic flux in the air-gap, resultingASX in higher torque density and it aligns with the high acceleration requirement used in the racing tracks [10].

Within this topic, this work intends to analyse the impact on the performance of electrical motors using VCoFe as magnetic core material.

As this is a multiphysics problem with non-linear materials and with a high number of variables and constraints, a multi-objective optimisation is done using a Non-dominated Sorting Genetic Algorithm II (NSGA-II) [11] to provide a general comparative analysis between VCoFe and FeSi materials for the application. This algorithm is used over a hybrid model of the motor where both analytical and Finite Element Method (FEM) are used, similar to the previous study done [9]. This approach has been proved to be a successful method in [11] taking less computational time than purely FEMs [12] while providing accurate enough results.

For this project, the introduced motor topology together with the hybrid model, offer accurate electromagnetic and thermal results as long as feasible times of computation. The motor's electromagnetic quantities are calculated with a stationary 2D FEM together with analytical expressions to estimate losses in the core and Permanent Magnet (PM)s and the estimated machine's operating temperature, which allow the optimisation of the EM and its increase of the current specific-power and efficiency limits.

II Background

The material selection for the different sections of the motor must be done to maximise the mechanical output power and, at the same time, to promote the machine's reliability.

II-A Motor Core Materials

The reliability of the developed motor will be achieved when the rotor can withstand the centrifugal forces and the electromagnetic materials operate securely in the operation temperature.

The production of heat coming from the different types of losses highly influences the motor temperature. The main temperature limiting factors are related to the withstanding temperature of the copper winding's insulation and of the PMs. The higher the temperature they can withstand, the higher will be the available peak and continuous torque and power.

The materials used on the motor and their properties considered in the electromagnetic and thermal models are defined below.

II-A1 Silicon-Steel Alloy (FeSi)

Silicon steel (NO15) is one of the possible magnetic core materials that can be used in the motor's rotor and stator. It is known as a soft magnetic material that is easy to magnetise and demagnetise along with low hysteresis losses. The main characteristics to consider are the saturation and the permeability that have a high influence on the maximum magnetic flux density and core losses, thus influencing the machine overall efficiency and power-density.

The material chosen for the model is *Silicon Steel NGO 35JN200* and its main properties can be seen in Table I, the parts of the machine corresponding to the NO15 material are the core of the machine, represented in Fig. 3 by the colour silver.

This magnetic core material is characterised by its respective B-H magnetic curve and specific loss curve obtained for a nominal frequency of 400 Hz, presented in Fig. 1, for laminations of 15 mm thickness. These curves were achieved by fitting data from the manufacturer's data-sheet.

Properties [Units]	**NO15**
Magnetic saturation [T]	1.6
Losses at 50 Hz with 1 T [W/Kg]	1.08
Losses at 400 Hz with 1 T [W/Kg]	12.1
Ultimate tensile strength [MPa]	450
Density [kg/cm^3]	7650

TABLE I: Properties of NO15.

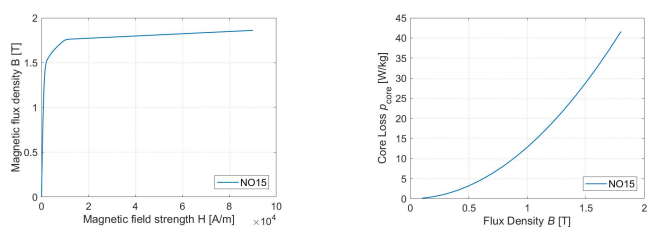

(a) B-H magnetisation curve (b) Specific losses curve

Fig. 1: Respective B-H magnetisation and specific losses curves for NO15.

II-A2 Vanadium-Cobalt-Iron Alloy (VCoFe)

The other possible choice for the magnetic core material of the machine is the main study of this project, Vanadium-Cobalt-Iron (VCoFe), an alloy with very high saturation point, low coercive field strength and low specific core losses. It overcomes NO15, on the linear zone, in means of higher saturation points (2.2-2.4 T) and higher relative magnetic permeability. However, VCoFe prices are higher and more volatile than the NO15, and for this reason, both materials will be studied for optimisation and better performances purposes.

The material chosen for the model is *Cobalt Steel Vacoflux 50* and its main properties can be seen in Table II The parts of the machine corresponding to the VCoFe material are the magnetic core of the machine, represented in Fig. 3 in silver colour.

Once again, this magnetic core material is characterised by its respective B-H magnetic curve and specific loss curve obtained for a nominal frequency of 400 Hz, presented in Fig. 2, also for laminations of 15 mm thickness to reach a better

comparison with NO15. These curves were achieved by fitting data from the manufacturer's data-sheet.

Properties [Units]	Vacoflux 50
Magnetic saturation [T]	2.35
Losses at 50 Hz with 1.5 T [W/Kg]	1.6
Losses at 400 Hz with 1.5 T [W/Kg]	31
Ultimate tensile strength [MPa]	350
Density [kg/cm^3]	8120

TABLE II: Properties of Vacoflux 50.

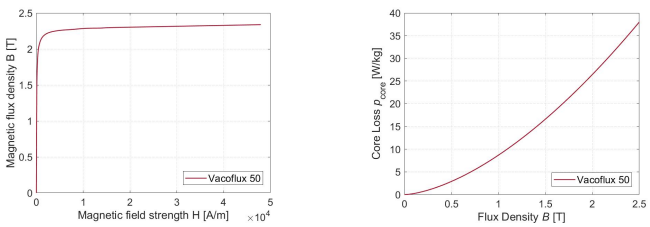

(a) B-H magnetisation curve (b) Specific losses curve

Fig. 2: Respective B-H magnetisation and specific losses curves for Vacoflux 50.

III Permanent Magnet Synchronous Machine Modelling

A detailed methodology for the studied EM is shown here based on an IPMSM, as well as the description of all the different components and characteristics.

III-A Base Topology

To start designing the base topology of the EM, its geometry and properties are studied as characteristic dimensions, as well as its motor materials and windings configuration. The characteristic dimensions of each part of the motor's magnetic core will be considered as decision variables for the optimisation process.

III-A1 Geometry

The EM is based on a spoke-type IPMSM with a flux-concentrating rotor design, with PMs magnetised alternately, along the angular coordinate. This base geometry is designed for demanding high-performance requirements and it was developed and validated for a 20 kW 8000 rpm IPMSM in [9]. In Fig. 3 a cross-section of a quarter of the proposed geometry can be observed where the PMs are presented in gold colour, the copper windings are presented in bronze colour, the air is presented in light blue colour and the magnetic core material is presented in grey colour.

The dimensions of the different components of the motor will determine the final motor design, being these used as decision variables in the optimisation process to maximise the IPMSM's torque and efficiency. These dimensions are the number of poles, number of phases, rotor radius, r_r, shaft radius, r_s, magnet width, w_m, magnet length, l_m, teeth width, w_t, teeth length, l_t, stator outer ring width, w_s, and air-gap size, g. These are presented also in Fig. 3.

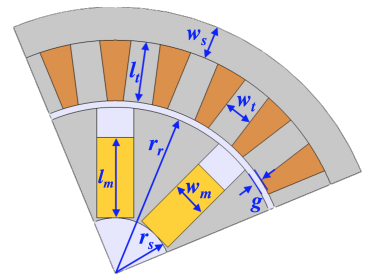

Fig. 3: IPMSM cross section and geometry dimensions.

III-A2 Winding Configuration

The fundamental magnetomotive force (mmf) establishes the quantity of flux moving between the rotor and the stator, being highly dependent on winding configuration and the length of the air-gap and having important weight on the motor torque. By minimising the harmonic fields the machine will have less torque ripple and higher efficiency consequently. The electrical balance is associated with the movement flow of the magnetic rotating waves on the air-gap.

The chosen configuration, in Fig. 4, was of 24 stator slots and 8 rotor poles, where in the stator, a single-layer concentrated winding layout was adopted to maximise the fundamental component of the air-gap magnetomotive force wave and to simplify the manufacturing process.

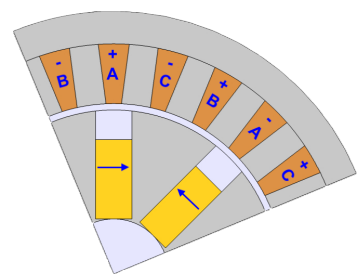

Fig. 4: Winding Configuration.

III-B Electromagnetic Modelling

The electromagnetic analytical modelling is based on the synchronous $d-q$ reference frame IPMSM's equivalent circuit considering iron losses, where its main parameters are obtained using a FEM tool. A hybrid analytical and FEM is used to represent the IPMSM to reduce the optimisation computational time to a feasible time. The optimisation can result in very high computational times due to its iterative process requiring a high number of simulations of the EM. This methodology will allow a good estimation of the main machine's equivalent circuit parameters of each tested geometry with a 2D stationary time simulation being used, as well as an estimate on the machine's performance for different operation points.

III-B1 $d-q$-Circuit

The equivalent electric circuit used is based on synchronous $d-q$ reference frame, presented in Fig. 5, where magnetic saturation effects are included through an equivalent resistance

and lumped parameters, such as $d-q$ inductance and iron core resistance, R_{Fe}, are estimated with results from static FEM.

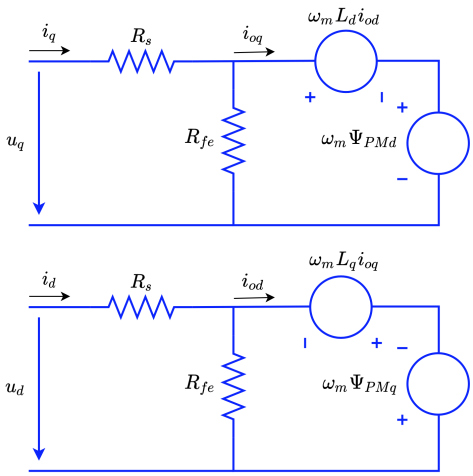

Fig. 5: d and q axes steady-state model in the rotor flux reference frame.

The steady-state equations that describe the three-phase machine, according to the equivalent circuits, are given in (1) to (4). The phase winding resistance R_s and the PM linked flux Ψ_{PM}, which for the considered machine topology is aligned with d-axis, represent the thermal variations since both are temperature dependent. The magnetic core effects are represented by the iron losses resistance, in the value of R_{Fe}, and the $d-q$ inductance's, L_d and L_q. ω_m is the rotor angular speed.

$$u_d = R_s i_d - \omega_m L_q i_{oq} - \cancel{\omega_m \Psi_{PM,q}} \tag{1}$$

$$u_q = R_s i_q + \cancel{\omega_m L_d i_{od}} + \omega_m \Psi_{PM,d} \tag{2}$$

$$\cancel{i_{od}} = i_d + \frac{\omega_m L_q i_{oq} + \cancel{\omega_m \Psi_{PM,q}}}{R_{fe}} \tag{3}$$

$$i_q = i_{oq} + \frac{\cancel{\omega_m L_d i_{od}} + \omega_m \Psi_{PM,d}}{R_{fe}} \tag{4}$$

To simplify the simulation of the electrical motor, a field-oriented control strategy was used, considering $i_{od} = 0$ and $\Psi_{PM,q} = 0$. This simplifies the machine's model equations and thus the calculation of the torque, T, decreasing the number of FEM simulations required and the computational time for the simulation, as the computation of L_d is not necessary anymore.

The steady-state torque, which has two components, the electromagnetic torque T_{EM} and reluctance torque T_{Rel} can be computed using (5), where T_{EM} was chosen to be optimised as it gives a good indication of the total torque of the machine.

$$\begin{aligned} T &= T_{EM} + \cancel{T_{Rel}} = \\ &= \frac{3}{2} n_{pp} (\Psi_{PM,d} i_{oq} - \cancel{\Psi_{PM,q} i_{od}} + \cancel{(L_d - L_q) i_{od} i_{oq}}) \end{aligned} \tag{5}$$

III-B2 Losses Calculation

The losses have a high impact in the motor efficiency and overall functioning and were divided in core losses, permanent magnet losses and copper losses. The estimation of core and PM's losses in IPMSMs is made by stationary approach so that the model can have the lowest computational time possible, as it will be used in the optimisation algorithm.

III-B2a Core Losses

Iron losses are roughly estimated by an aggregate of three components: hysteresis losses, eddy current losses and excitation losses, obtained from loss curve data provided by the manufacturer, considering a sinusoidal variation of the flux density between the d and q axes, in the rotor and stator cores. Hysteresis losses take into consideration the B-H curve, eddy current losses include the currents induced by the electromotive force generated in the stator core and excitation losses regards to the synchronous state of the EM.

Besides neglecting the effects of harmonics, the effects of minor loops and Direct Current (DC) bias on hysteresis losses on the rotor core, are also ignored [12].

In (6) core loss density, p_{core}, is calculated with Steinmetz equation, where K_{hyst}, K_{eddy} and K_{exci} are the hysteresis, eddy current and excitation losses coefficients respectively and are obtained from loss curve data, considering sinusoidal variation of the flux density in the rotor and stator cores.

$$p_{core} = K_{hyst} B^2 f + K_{eddy} (Bf)^2 + K_{exci} (Bf)^{1.5} \tag{6}$$

Where B is the amplitude of magnetic flux density, obtained from FEM of the cases where stator flux is aligned with d and q rotor's axes, and f is the frequency of the flux density.

III-B2b Permanent Magnets Losses

With the purpose of reducing eddy-current losses in the PMs, to improve the machine's performance and decrease the risk of demagnetisation, an analytical model to calculate the losses density in the PMs was applied [13]. Such model, calculated in (7), is a valid analytical approximation for parallelepiped shaped PMs while neglecting skin effect.

$$p_{PM} = \frac{\pi^2 f^2 B^2}{8 \rho_{PM}} \frac{l_m^2 L_{motor}^2}{l_m^2 + L_{motor}} \tag{7}$$

After the computation of the core and PM's losses density, these are used in (8) to calculate the equivalent iron losses resistance, R_{fe}.

$$R_{fe} = \frac{3}{2} \frac{(\omega_m (L_d i_{od} + \Psi_{PM}))^2 + (\omega_m L_q i_{oq})^2}{\rho_{core} V_{core} + \rho_{PM} V_{PM}} \tag{8}$$

III-B2c Copper Losses

The phase winding's resistance R_s can be estimated from (9).

$$R_s = N_{turns}\frac{l_{cu}}{A_{\varnothing}\rho_{cu}} = \frac{f_w A_{slot}}{N_{par}}\frac{l_{cu}}{\rho_{cu}(A_{\varnothing})^2} \tag{9}$$

The copper winding's losses are then obtained in (10), in function of the phase winding's resistance, R_s. Where i_d and i_q are the d and q axes currents and R_s the phase winding resistance.

$$P_{copper} = \frac{3}{2}R_s(i_d^2 + i_q^2) \tag{10}$$

III-B3 Finite Element Model (FEM)

A FEM of the synchronous machine was developed to calculate the magnetic flux distribution and magnetic inductance originated for each geometry. Therefore, the use of optimisation tools has been allowing the improvement of EM's performance, the increase of their current power density and efficiency limits.

III-B3a Periodic Conditions

From the machine's symmetry, it was possible to reduce the simulation of the whole machine into one-quarter, simulating only one pole pair of the machine as in Fig. 6. This reduction was used during the project to perform all the computational calculations and optimisation process with reduced complexity and within a feasible computation time of the model.

In Fig. 6 it is observed a periodic continuity condition being applied to the internal boundaries, where the geometry was sliced along the flux density distribution, so the results would be the same as using the entire geometry.

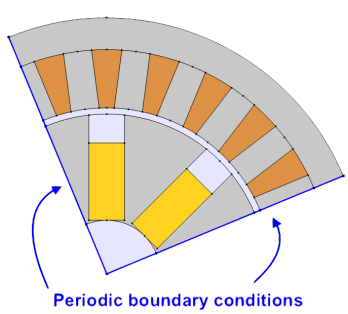

Fig. 6: Cross section of geometry sliced.

III-B3b Coil Flux Calculation

From the analysis of a generic topology of the IPMSM, and for the considered number of poles and stator slots, the direct and quadrature axes, $d-q$, are $\theta_{me} = 0°$ and $\theta_{me} = 22.5°$, respectively. This can be seen in Fig. 7 in blue colour.

A stationary-time simulation for the $d-q$ axes is considered and the current in each phase is given by (11).

$$i_A = I_m cos(\omega t) \tag{11a}$$

$$i_B = I_m cos(\omega t - 2\pi/3) \tag{11b}$$

$$i_C = I_m cos(\omega t + 2\pi/3) \tag{11c}$$

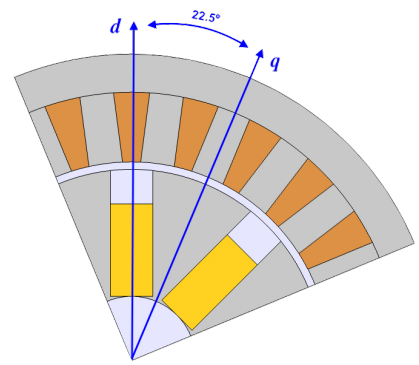

Fig. 7: Representation of rotor's d and q axes.

Depending if the rotor's q and d axes are aligned with phase A, the Park transformation results in $i_{od} = 0$ and $i_{oq} = I_m$ or $i_{od} = I_m$ and $i_{oq} = 0$, respectively.

To calculate the magnetic flux on both direct and quadrature axes, adjusting the rotor's position with the d and q axes, two calculations were made, to estimate from the FEM simulations the $d-q$ linked fluxes, Ψ_d and Ψ_q, and the flux density distributions, B_d and B_q.

First, the rotor was considered without the PM's flux ($Br = 0$) and the stator current density was imposed, from zero to a maximum value defined by the optimisation tool, to calculate the winding's linkage flux in both axis, d and q. This allows the calculation of the L_d and L_q parameters.

The second calculation was made considering the rotor PMs ($B_r = 1.2$ T) with zero induced current density ($J = 0$) with the PM flux aligned with the d-axis, to allow the calculation of the PM's d-axis linkage flux, $\Psi_{PM,d}$.

The estimation of R_{fe} in (8) from the locked rotor core losses method depends on the amplitude of the flux density B_m in the PMs, rotor and stator, calculated in (12). B_d and B_q are obtained by simulations with the stator flux aligned with d and q rotor axes and with $\Psi_{PM} \neq 0$.

$$B_m = |B_d - B_q| \tag{12}$$

III-B3c Inductance Calculation

L_d and L_q inductances are computed in (13) from results of linked flux acquired, following the previous procedure, using the FEM. With PMs flux Ψ_{PM} reduced to zero (Ψ_{PM} =0), the stator is aligned with the rotor's d and q axes in positions of maximum and minimum flux linkage, respectively. Ψ_d and Ψ_q are acquired in function of i_d and i_q currents and for simplification, saturation is neglected.

$$L_d = \left.\frac{\Psi_d}{i_{od}}\right|_{i_{oq}=0} \qquad L_q = \left.\frac{\Psi_q}{i_{oq}}\right|_{i_{od}=0} \tag{13}$$

III-B3d Magnetic Flux Distribution

To avoid magnetic saturation and to limit the operation temperature of the materials, the following limits are imposed:

- $B_{Sat}(FeSi) = 1.6$ T Maximum flux density for FeSi

- $B_{Sat}(VCoFe) = 2.2$ T Maximum flux density for VCoFe
- $T_{amb} = 30$°C Room temperature
- $T_s = 120$°C Maximum surface temperature

Two *Line Maximum* operations were done to calculate the maximum magnetic flux density in the stator along strategic lines represented in Fig. 8 in blue colour.

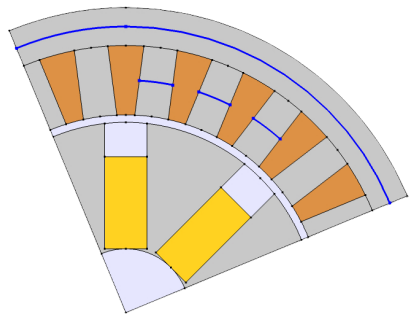

Fig. 8: Magnetic flux density norm calculation in the stator.

Two *Surface Average* operations were done to calculate the magnetic flux density norm on the rotor. One surface is the core of the rotor and the other the PMs, as the non-uniform distribution on those domains makes it difficult to be characterised by a line. If the maximum flux density in these chosen segments on the stator or the average flux density rotor and PMs values are above a certain threshold, the core is considered to violate the magnetic constraint. This method is used to avoid localised peaks of high flux concentration resulting in the rejection of promising geometries during the optimisation.

III-C Thermal Model

It is important to have a thermal model capable of predicting the machine's operating temperature for a set of electric variables, such as current, frequency and magnetic flux. This thermal model will enable the discard of designs which overpass thermal limits as well as assess safety thermal margins of each optimised solution.

A simplified thermal model is considered to estimate the maximum operating point of the machine, with a single heat transfer coefficient representing the heat dissipation from the machine to the cooling system. The thermal model will be integrated in the model's optimisation so it must be computationally fast and sufficiently accurate. The machine is considered as a cylinder that produces heat resulting from Joule losses in the rotor core, (6) and PMs, (7), which is dissipated through the air-gap and, together with the stator and copper winding's losses, (10), trough the cooling jacket and into the environment. Considering that the motor will be required to provide nominal power in short bursts, the maximum operating steady state temperature can be estimated for the worst-case scenario to evaluate if the optimisations are viable.

The opted cooling system achieves a heat transfer coefficient of h =1000 Wm^{-2}k^{-1} and can be observed in Figure 9. The estimation considers convective heat transfer in the air-gap and dissipation from the machine's surface to the cooling system environment.

Thermal conduction in the rotor and stator core are neglected as the conductive thermal resistance in metallic materials is very low when compared to the convective ones. The machine produces heat from Joule losses in the rotor core, (6) and PMs, (7), which is dissipated through the air-gap and, together with the stator and copper winding's losses, (10), trough the cooling jacket and into the environment.

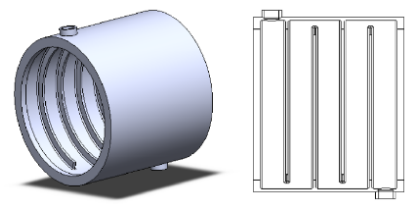

Fig. 9: Motor sleeve with chicane piping layout [14].

The heat transfer is described by the thermal equation (14) where T_s and T_{amb} are the surface and ambient temperatures, h is the transfer coefficient, S is the machine's surface area and P_{core}, P_{PM}, P_{copper} are the magnetic core, PMs and copper losses, respectively.

$$(T_s - T_{amb}) = \frac{1}{hS}(P_{core} + P_{PM} + P_{copper}) \tag{14}$$

IV Multi-Objective Optimisation

The geometry of the EM is here optimised and the results from using VCoFe and FeSi are compared.

IV-A Genetic Algorithm - NSGA-II

For EMs, multi-objective optimisation is important from the point of view of practical problem-solving. Instead of a single optimal solution, it provides a set of optimal solutions for the design of the machine. This multi-objective optimisation is coupled with a FEM and analytical expressions, due to the multiphysics involved, which are interdependent with non-linear materials.

NSGA-II [11] was the chosen genetic algorithm. This algorithm allows the optimisation of various objective functions, with several constraints, using a fast and elitist approach where the best solutions of each generation are preserved to be optimised on the next generation and a diversity preserving mechanism is used, improving the diversity among solutions of the same non-dominated front.

IV-B Design Optimisation

IV-B1 Objective Functions

Since the aim is to compare FeSi and VCoFe as material core for the spoke-type IPMSM FST's car, the objective is to reach the electromagnetic torque maximisation, T_{EM} and, since this one is limited by the decision variables and the constraints, it is directly related with the efficiency maximisation, η, resulting

in a multi-objective optimisation and therefore the results are presented by a 2D curve of T_{EM} vs η.

As such, the objective functions are:

$$f_{1,2}(x) = \begin{cases} \min(-T_{EM}) \\ \min(-\eta) \end{cases} \equiv \begin{cases} \max(T_{EM}) \\ \max(\eta) \end{cases} \tag{15}$$

To reduce the computational time, a simplification of the machine's model equations was done, The electromagnetic component of the generated torque was calculated in (16) as a good indication of the total torque of the machine.

$$f_1(x) = T_{EM} = \frac{3}{2} n_{pp} \Psi_{PM} i_{oq} \tag{16}$$

The objective function concerning the efficiency is calculated in (17).

$$f_2(x) = \eta = \frac{T_{EM}\omega_M}{T_{EM}\omega_M + \rho_{core}V_{core} + \rho_{PM}V_{PM}} \tag{17}$$

IV-B2 Decision Variables

The DNA of each individual is an optimisation vector, with nine different decision variables, that generates values for the objective functions. These decision variables are the torque producing current density of the $q-axis$, J, and the geometry dimensions of the rotor radius, shaft radius, magnet width, magnet length, teeth width, teeth length, outer stator width and air-gap size. Resulting in an optimisation vector of nine decision variables, $\boldsymbol{x} = [J, r_r, r_s, w_m, l_m, w_t, l_t, w_s, g]$.

The boundary's limits for dimensions in Fig. 3 are presented in Table III.

Variable	Description	Boundaries
J	Current density	1-40 [MA/m^2]
r_r	Rotor radius	20-40 [mm]
r_s	Shaft radius	5-30 [mm]
w_m	Magnet width	1-15 [mm]
l_m	Magnet length	5-20 [mm]
w_t	Tooth width	1-10 [mm]
l_t	Tooth length	7-20 [mm]
w_s	Outer stator width	1-20 [mm]
g	Air-gap	1-1.5 [mm]

TABLE III: Geometry dimension's boundaries.

IV-B3 Constraints

Not only the dimension's boundaries had to be taken into account but also the manufacturing feasibility of the motor, with the optimised geometry. In table IV, the constraints considered regarding geometrical dimensions and weight are presented, as well as inverter's, thermal and magnetic limits.

The geometrical constraints are simply imposed by the user according to application-specific requirements, such as maximum dimensions and weight, whereas thermal limitations and magnetic constraints are reliant on the magnetic saturation of the chosen core material, leading to less efficient geometries, and temperature safety, protecting PMs and winding isolation. The inverter's constraint is merely its limit of operation.

	Design constraints	Constraint values
Geometrical	Weight	5 kg
	Outer radius of the motor	50 mm
	Stack length of the motor	80 mm
Inverter	Peak currrent	100 A
Thermal	Copper winding's temperature	180°C
	Permanent magnet's temperature	120°C
Magnetic	Magnetic flux density for FeSi	<1.6 T
	Magnetic flux density for VCoFe	<2.2 T

TABLE IV: Design constraints.

V Results

The final optimisation results are afterwards presented, both for VCoFe and FeSi, and described for the optimised last generation of the NSGA-II algorithm.

V-A Preferred Working Area

To have the model design operating in the best saturation point, whether aiming for a riskier but more efficient region or a safer but less efficient region, three different machines were were optimised with different constraints regarding the maximum magnetic flux density.

A clear relation between the torque and the magnetic flux constraint can be observed in the Pareto front of Fig. 10. Where an increase in the maximum allowed magnetic flux generates higher efficiency.

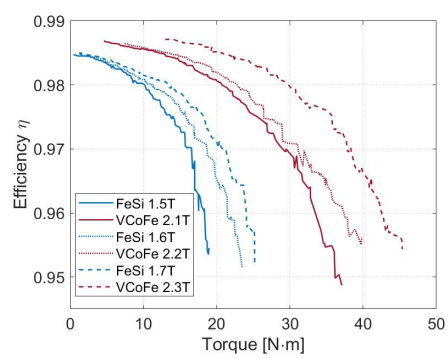

Fig. 10: Pareto front.

In Fig. 11 the linked magnetic flux in the PMs regarding the direct axis is observed for the three different designs. Contrarily to the efficiency, the linked magnetic flux does not represent a noteworthy improvement with the increase of the maximum magnetic flux.

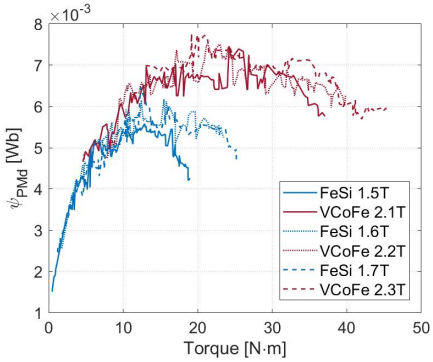

Fig. 11: Linked flux in the PMs with $d-axis$ orientation.

Regarding this results, the maximum magnetic flux constraint elected for the optimisation of the model design machine was <1.6 T and <2.2 T, for FeSi and VCoFe respectively. With the objective of reaching a remarkable torque and efficiency value with a lower risk of magnetisation.

V-B Optimisation Results

The optimisation was done regarding both FeSi and VCoFe materials separately, using a genetic NSGA-II population of 200 elements and 150 generations for each optimisation with the solutions arranged increasingly by its torque.

The final Pareto front obtained for the maximisation of the torque and efficiency, from the last generation, is presented in Fig. 12, with every solution meeting all the constraints. Where VCoFe outperforms FeSi in an estimated increase of up to 3% in efficiency for the same torque, or up to 70% torque increase for the same efficiency level. For the FST competition car, with a required 20 Nm of nominal torque, there is an efficiency increase of 1.7%.

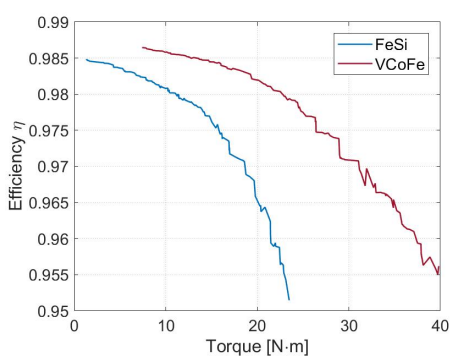

Fig. 12: Pareto front of the last population optimisation.

Is shown in figures 13(a) and 13(b) the magnetic and thermal constraints being met, with J_{th} corresponding to the maximum current allowed, limited by the thermal constraints. As the magnetic flux density on both solution is at the maximum value, 1.6 T and 2.2 T for FeSi and VCoFe respectively, the magnetic constraint is the limiting factor.

In Fig. 14 the core and copper losses of the machines are presented. Is possible to identify in Fig. 14(a) the same

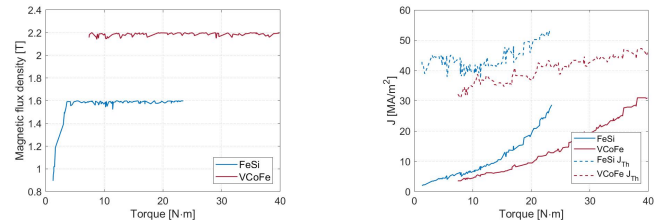

(a) Magnetic flux density (b) Thermal current density

Fig. 13: Magnetic and thermal constraints.

approximate losses in both machine cores, with slight inferior results for the FeSi machine. Regarding winding copper losses, it is clear in Fig. 14(b) that VCoFe outperforms FeSi with remarkable reduced losses.

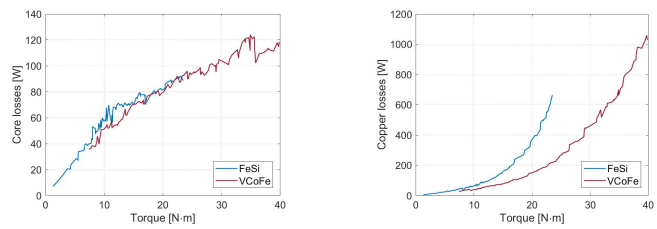

(a) Core losses (b) Copper losses

Fig. 14: Core and copper losses.

In Fig. 15 can be noted that the torque increases with current density, J, for both materials. PMs dimensions, in figures 16(c) and 16(d), are at the maximum possible for each geometry to maximise linked flux and torque. VCoFe achieves higher magnet widths, consequently resulting in more magnetic flux.

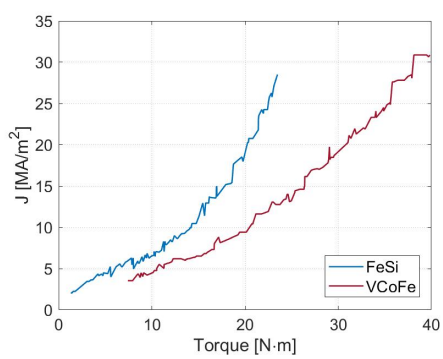

Fig. 15: Current density.

Reaching high current densities to maximise torque, outcomes in dimensions modifications with the purpose of keeping the magnetic flux density around constraint level, resulting in a decrease of efficiency and an increase of the core volume. This can be seen in Fig. 17(a), where, for the same torque value, the core volume of the VCoFe machine is around 10% smaller than the machine of the FeSi optimisation. For the FST competition car, with a required 20 Nm of nominal torque,

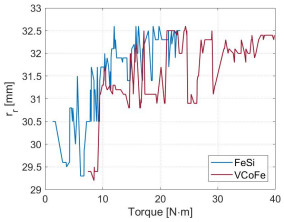

(a) Rotor radius, r_r

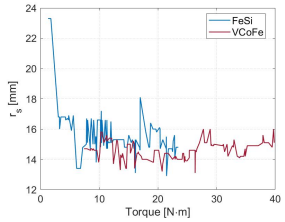

(b) Shaft radius, r_s

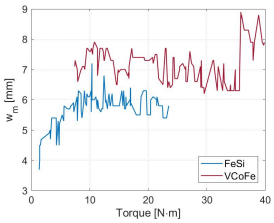

(c) Magnet width, w_m

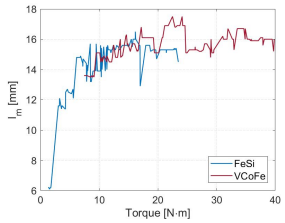

(d) Magnet length, l_m

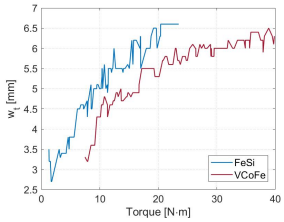

(e) Teeth width, w_t

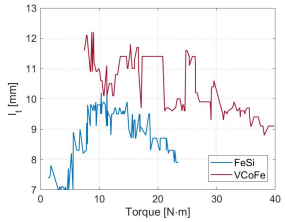

(f) Teeth length, l_t

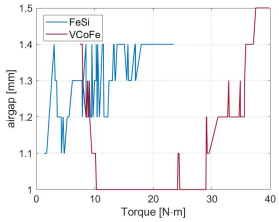

(g) Air-gap length, gap

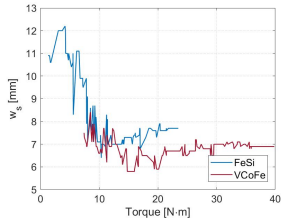

(h) Stator outer ring width, w_s

Fig. 16: Dimensions optimisation.

there is a reduction of 11% in core volume for the motor.

Nevertheless, due to the material density being higher for the VCoFe alloy, 8120 kg/m^3, than FeSi alloy density, 7650 kg/m^3, this difference is not noticeable in core weight, Fig. 17(b).

In respect of this, torque density for both core materials is similar for similar torque regions, however, since it is possible to achieve higher torque densities with higher nominal torque with VCoFe material, these machines present increased torque with similar weights, compared to FeSi machines from lower torque ranges.

In Fig. 18 a final optimised solution for the machine reaching $T = 20$ Nm, as required for the FST, is presented both for FeSi and VCoFe. Where the coloured bars represent the magnetic saturation. The final optimised dimensions for this solutions can be seen in table V.

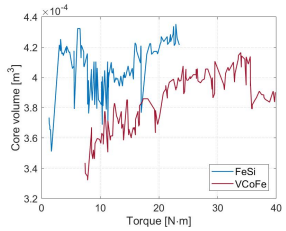

(a) Core volume

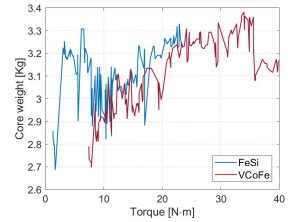

(b) Core weight

Fig. 17: Volume and Weight of the machine optimisation.

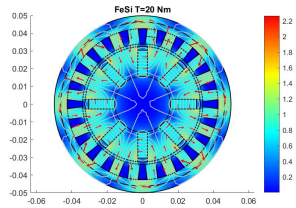

(a) FeSi simultation

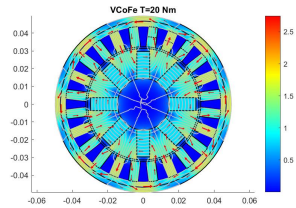

(b) VCoFe simulation

Fig. 18: Optimised solution for $T = 20$ Nm.

Variable	Description	FeSi	VCoFe
J	Current Density	17.98	9.41 [MA/m^2]
r_r	Rotor radius	32.6	31.4 [mm]
r_s	Shaft radius	15.8	14.6 [mm]
w_m	Magnet width	05.5	07.3 [mm]
l_m	Magnet length	14.7	15.1 [mm]
w_t	Tooth width	06.0	05.3 [mm]
l_t	Tooth length	08.7	11.4 [mm]
w_s	Outer stator width	07.3	05.9 [mm]
g	Air-gap	01.4	01.0 [mm]

TABLE V: Optimised geometry dimensions for $T = 20$ Nm.

VI Conclusions

The main objective of this project was to define where using VCoFe alloy, holding a remarkable high saturation point of 2.2-2.4 T, provides an advantageous utilisation in a high specific-power spoke-type IPMSM for the worldwide competition's FST electric car, demanding high-performance requirements with a large ratio of power/volume. The typical FeSi and the newly used VCoFe metallic alloys have been considered as the magnetic core material of the EM, to provide a general comparative analysis between the two of them.

The main literature on the use of PMSM in an electric racing car and other specific traction application, along with the different possible materials used in the manufacturing of an EM is reviewed. The manufacturing and post-processing various procedures and techniques were analysed and how it affects the final magnetic properties. Different magnetic circuits geometries were designed and studied to meet the FST performance specifications and defined requirements.

Due to the multiphysics complexity (electromagnetic, mechanical and thermal, with non-linear materials) and to high number of variables and constraints, a multi-objective opti-

misation was applied with NSGA-II algorithm coupled with a hybrid analytical/FEM to provide sufficiently accurate electromagnetic and thermal results within a feasible time. This approach allowed to identify the best parameters and machine designs, using VCoFe and FeSi, regarding the two objective functions of maximising torque production and efficiency, while fulfilling the relevant applicable constraints. A visualisation of the Pareto front and the analysis of the different variables along the optimised solutions is additionally possible with the use of this optimisation's algorithm.

Each genetic optimisation was done for 150 generations with 200 population elements each, meaning that 30000 different motor geometries were tested, which was enough for the solution to converge within a feasible time of 26 hours for FeSi and 30 hours for VCoFe, due to the low computational time of the developed electromagnetic and thermal model.

The developed hybrid model is composed of a stationary time 2D FEM, to calculate the motors main parameters such as $d - q$ inductances and magnetic flux distribution, and an auxiliary analytical script to compute voltage, losses, electromagnetic torque and efficiency. The electromagnetic and thermal model's investigation was conducted applying each material's B-H magnetisation curve and losses, to increase the motor's reliability and performance, where the opted cooling system to apply was previously developed in a preceding study.

Results from the Pareto front demonstrate VCoFe as a beneficial core material choice across both torque and efficiency ranges, while providing higher power densities than FeSi. Outperforming FeSi in an estimated increase of up to 3% in efficiency for the same torque, or up to 70% torque increase for the same efficiency level. For the competition car, with a required 20 Nm of nominal torque, there is an efficiency increase of 1.7% and a reduction of 11% in the magnetic core volume for the motor. Enabling the motor optimised with VCoFe to reach up to 40 Nm where, for the same available space and with similar levels of efficiency, FeSi only reaches 24 Nm. However, due to the higher material density of VCoFe, a more tenuous variation in core weight is observed, compared to FeSi.

Analysing each of the decision variables, it is possible to determine that the performance of the motor is limited by the saturation curve of the ferromagnetic material, however, due to the cooling system applied, it has high thermal safety margin.

Therefore, it can be concluded that using VCoFe alloy as a core material has a high impact on the efficiency and global performance of the motor. Appearing to be a great option for the core material of traction motor applications where the volume and performance overcome the importance of the final price, as in aeronautical and, as the FST, racing environment.

References

[1] T. V. Jayaraman, "Effect of Processing of HIPERCO® 50 Alloy Laminates on Their Magnetic Properties," *Journal of Electronic Materials*, vol. 44, no. 11, pp. 4379–4386, 2015.

[2] B. A. Krings, M. Cossale, A. Tenconi, J. Soulard, A. Cavagnino, and A. Boglietti, "Magnetic Materials Used in Electrical Machines," *IEEE Industry Applications Magazine*, vol. 23, no. 6, pp. 21–28, 2017.

[3] A. Krings, A. Boglietti, A. Cavagnino, and S. Sprague, "Soft Magnetic Material Status and Trends in Electric Machines," *IEEE Transactions on Industrial Electronics*, vol. 64, no. 3, pp. 2405–2414, 2017.

[4] X. Zhang and K. S. Haran, "High-specific-power electric machines for electrified transportation applications-technology options," *ECCE 2016 - IEEE Energy Conversion Congress and Exposition, Proceedings*, 2016.

[5] M. Palmieri, M. Perta, and F. Cupertino, "Design of a 50.000-r/min synchronous reluctance machine for an aeronautic diesel engine compressor," *IEEE Transactions on Industry Applications*, vol. 52, no. 5, pp. 3831–3838, 2016.

[6] N. Fernando, G. Vakil, P. Arumugam, E. Amankwah, C. Gerada, and S. Bozhko, "Impact of Soft Magnetic Material on Design of High-Speed Permanent-Magnet Machines," *IEEE Transactions on Industrial Electronics*, vol. 64, no. 3, pp. 2415–2423, 2017.

[7] B. C. Mecrow, A. G. Jack, D. J. Atkinson, S. R. Green, G. J. Atkinson, A. King, and B. Green, "Design and testing of a four-phase fault-tolerant permanent-magnet machine for an engine fuel pump," *IEEE Transactions on Energy Conversion*, vol. 19, no. 4, pp. 671–678, 2004.

[8] N. Volbers and J. Gerster, "High Saturation , High Strength Iron-Cobalt Alloy for Electrical Machines," *Proceedings of the INDUCTICA, CWIEME*, pp. 1–4, 2012.

[9] P. P. C. Bhagubai, J. G. Sarrico, J. F. P. Fernandes, and P. J. C. Branco, "Multi-Objective Optimization, and Prototyping of a 20 kW 8000 rpm Permanent Magnet Synchronous Motor for a Competition Electric Vehicle," *Energies*, vol. 13, no. 10, p. 2465, 2020.

[10] B. K. Lee, G. H. Kang, J. Hur, and D. W. You, "Design of spoke type BLDC motors with high power density for traction applications," *Conference Record - IAS Annual Meeting (IEEE Industry Applications Society)*, vol. 2, pp. 1068–1074, 2004.

[11] K. Deb, A. Pratap, S. Agarwal, and T. Meyarivan, "A fast and elitist multiobjective genetic algorithm: NSGA-II," *IEEE Transactions on Evolutionary Computation*, vol. 6, no. 2, pp. 182–197, 2002.

[12] S. H. Han, T. M. Jahns, and Z. Q. Zhu, "Analysis of rotor core eddy-current losses in interior permanent-magnet synchronous machines," *IEEE Transactions on Industry Applications*, vol. 46, no. 1, pp. 196–205, 2010.

[13] W. Y. Huang, A. Bettayeb, R. Kaczmarek, and J. C. Vannier, "Optimization of magnet segmentation for reduction of eddy-current losses in permanent magnet synchronous machine," *IEEE Transactions on Energy Conversion*, vol. 25, no. 2, pp. 381–387, 2010.

[14] P. M. d. A. Fontes, "Refrigeração do propulsor elétrico de um veículo Formula Student," Ph.D. dissertation, Técnico Lisboa, 2016.

=2